A search for the radio counterpart of the unidentified γ-ray source 3EG J1410–6147

M. Doherty,[1][⋆][†] S. Johnston,[1] A. J. Green,[1] M. S. E. Roberts,[2] R. W. Romani,[3] B. M. Gaensler[4] and F. Crawford[5]

[1]*School of Physics, University of Sydney, NSW 2006, Australia*
[2]*Department of Physics, McGill University, Montreal, Quebec H3A2T8, Canada*
[3]*Department of Physics, Stanford University, Stanford, CA 94025, USA*
[4]*Harvard-Smithsonian Centre for Astrophysics, Cambridge, MA 02138, USA*
[5]*Department of Physics, Haverford College, Haverford, PA 19041, USA*

ABSTRACT

We have made radio continuum, H I and X-ray observations in the direction of the unidentified EGRET source 3EG J1410–6147, using the Australia Telescope Compact Array and the *Chandra* X-ray Observatory. The observations encompass the supernova remnant (SNR) G312.4–0.4 and the two young pulsars PSRs J1412–6145 and J1413–6141.

We derive a lower distance limit of 6 kpc to the SNR, although interpretation of positive velocity features in the H I spectrum may imply that the SNR is more distant than 14 kpc. PSR J1412–6145, with an age of 50 kyr, is the pulsar most probably associated with SNR G312.4–0.4. X-rays are not detected from either pulsar and diffuse X-ray emission near the bright western edge of the SNR is weak. Although there is circumstantial evidence that this western region is a pulsar wind nebula (PWN), the embedded pulsar PSR J1412–6145 is apparently not sufficiently powerful to explain the radio enhancement. The origin of the electron acceleration in this region and of the γ-rays remains unidentified, unless the distance to PSR J1413–6141 is at least a factor of 3 lower than its dispersion measure distance.

Key words: pulsars: individual: J1412–6145 – pulsars: individual: J1413–6141.

1 INTRODUCTION

Since the discovery of the first unresolved γ-ray source some 30 years ago, a large number of high-energy sources remain without obvious counterparts at other wavelengths. In the third EGRET catalogue of γ-ray sources (Hartman et al. 1999) there are ∼170 sources that are as yet unidentified. There have been a variety of approaches used in attempting to determine the nature of these unidentified sources. However, owing to very large positional uncertainties for EGRET sources (of the order of 1°), identifying counterparts at other wavelengths is problematic, particularly in the Galactic plane where the surface density of sources is high. The most powerful technique for identifying sources at other wavelengths is a detailed multiwavelength study of individual sources (e.g. Roberts et al. 2001a).
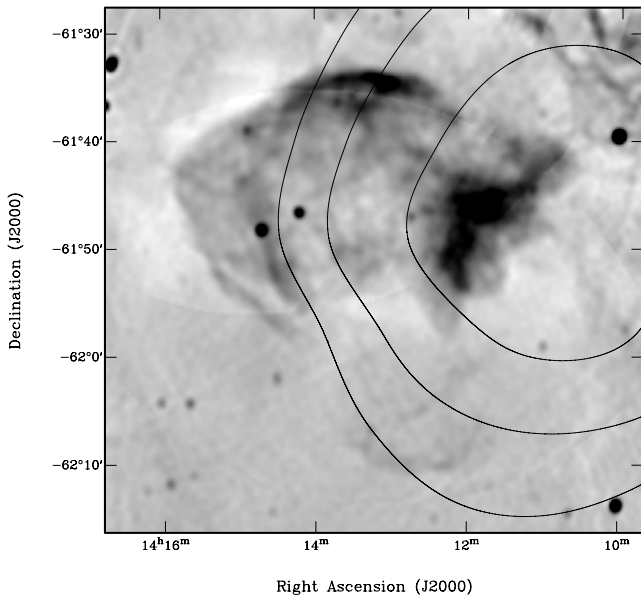
There are two γ-ray sources in the southern Galactic plane near longitude 312°. Observations of 2EGS J1418–6049 at radio and X-ray wavelengths have shown that it is probably associated with the young radio and X-ray pulsar PSR J1420–6048 (Roberts, Romani &

Johnston 2001b). A hard X-ray source embedded in a radio nebula, possibly a pulsar wind nebula (PWN) may also contribute to the γ-ray flux (Roberts et al. 1999). The second γ-ray source, 3EG J1410–6147 (2EGS J1412–6211), was tentatively linked with the supernova remnant (SNR) G312.4–0.4 as the most plausible radio counterpart (Hartman et al. 1999). This association was discussed by Case & Bhattacharya (1999), but they did not reach any definitive conclusions, merely speculating that the γ-ray emission could be a result of either emission from a PWN within the SNR or the acceleration of cosmic rays by the supernova shock.

SNR G312.4–0.4 was discovered by Caswell & Barnes (1985) who estimated a lower distance limit of 3.8 kpc from H_2CO absorption measurements. SNR G312.4–0.4 appears in the Molonglo Observatory Synthesis Telescope (MOST) SNR catalogue (Whiteoak & Green 1996) and in a detailed study of this region with the MOST at 843 MHz by Whiteoak, Cram & Large (1994). At this frequency, the SNR has a horseshoe-like morphology, with weaker emission in the south. There is a faint arc of emission approximately 12 arcmin to the south of the remnant, presumably a blow-out of part of the shell. Observations have also been made at 4.5 and 8.55 GHz with the Parkes radio telescope of both total and linearly polarized intensity (Whiteoak 1993). The eastern boundary and the western

⋆E-mail: md@ast.cam.ac.uk
†Present address: Institute of Astronomy, Madingley Rd, Cambridge CB3 OHA.

Figure 1. MOST image of SNR G312.4–0.4 at 843 MHz (Whiteoak & Green 1996), overlaid with EGRET confidence contours at 68, 95 and 99 per cent (Hartman et al. 1999).

2 OBSERVATIONS

2.1 Radio observations

Radio observations of SNR G312.4–0.4 were made with the Australia Telescope Compact Array (ATCA; Frater, Brooks & Whiteoak 1992). The ATCA is an east–west synthesis telescope located near Narrabri, NSW and consists of six 22-m antennas on a 6-km track. Five of the antennas are movable along the track, enabling observations to be carried out in configurations of different baselines between 31 m and 6 km. The ATCA can observe at two different frequencies simultaneously and is capable of recording all four Stokes parameters at each frequency.

Our observations consist of two separate pointings and were obtained over six observing sessions, with four different array configurations, 6D, 1.5A, 750C and 375. Details are given in Table 2. Each observation was for 12 h. Antenna 1 was not functioning during the observations on 2001 January 9; hence, only 10 baselines were recorded.

Our observations comprise continuum data split into 32 channels, each of 4 MHz, for a total bandwidth of 128 MHz centred on 1384 MHz, and H I data with a 4-MHz bandwidth and 1024 channels, centred on 1420 MHz. All Stokes parameters were recorded for the continuum data, enabling polarization parameters to be calculated. The H I observations were made only in total intensity.

2.2 X-ray observations

We obtained a 9.7-ks exposure of G312.4–0.4 with the *Chandra* X-ray Observatory on 2001 July 26, with pointing centre RA (J2000) $14^h12^m6^s.52$, Dec. (J2000) $-61°45'44''.8$. The four ACIS-I chips, together with two chips from the ACIS-S array provide significant coverage of the SNR (see Fig. 5, below). The data were reduced with standard procedures from the CIAO 2.2.1 package. No large background flares were observed during this exposure, so the full time interval was incorporated into the final maps.

enhancement of the SNR were found to be strongly polarized at 8.55 GHz (∼10–20 per cent), while lower levels of polarization were found at 4.5 GHz (∼2–5 per cent). This is potentially indicative of a PWN. Fig. 1 shows the MOST image of the SNR overlaid with the 68, 95 and 99 per cent confidence contours for the position of 3EG J1410–6147.

There are three pulsars within the 99 per cent confidence limits for the position of 3EG J1410–6147, all recently discovered by the Parkes Multibeam Survey (Manchester et al. (2001) and http://www.atnf.csiro.au/research/pulsar/catalogue). Table 1 lists their position, period (P), period derivative ($\dot{P}$), characteristic age (given by $P/2\dot{P}$), dispersion measure (DM), distance (d) determined from the DM using the electron density model of Cordes & Lazio (2002) and spin-down energy ($\dot{E}$). The DM-determined distances are known to be problematic in this part of the Galactic plane (Johnston et al. 2001) and are likely to be uncertain by a factor of 2. The two young pulsars both lie (in projection at least) within the SNR shell and are potential counterparts for 3EG J1410–6147.

Given the presence of young, energetic pulsars, the SNR and a putative PWN, we undertook radio and X-ray observations of this region. The radio observations were primarily aimed at determining an H I kinematic distance to the SNR. A known distance then enables us to consider the energetics of the system. In X-rays we hoped to detect the young pulsars and hence unravel the nature of the SNR and its PWN.

Table 2. ATCA observations of SNR G312.4–0.4.

Date	Array config.	Pointing centre (J2000) RA	Dec.	ν_1 (MHz)	ν_2 (MHz)
1998 Nov 1	6D	$14^h 13^m 22^s$	$-61°33'31''$	1384	
1999 Nov 27	375	$14^h 13^m 22^s$	$-61°33'31''$	1384	
1999 Dec 17	1.5A	$14^h 13^m 22^s$	$-61°33'31''$	1384	
2001 Jan 9	750C	$14^h 12^m 00^s$	$-61°47'30''$	1384	1420
2001 Jan 12	750C	$14^h 12^m 00^s$	$-61°47'30''$	1384	1420
2001 Feb 25	375	$14^h 12^m 00^s$	$-61°47'30''$	1384	1420

Table 1. Properties of three radio pulsars in the error box of 3EG J1410–6147.

Name	RA J2000	Dec J2000	P (s)	$\dot{P}$ ($\times 10^{-15}$) (s s^{-1})	Age (kyr)	DM (pc cm^{-3})	d (kpc)	$\dot{E}$ ($\times 10^{34}$) (erg s^{-1})
PSR J1407–6153	$14^h 07^m 57^s$	$-61°53'59''$	0.7016	8.85	1250	645	9.7	0.12
PSR J1412–6145	$14^h 12^m 08^s$	$-61°45'29''$	0.3152	98.65	50.6	515	7.8	12.4
PSR J1413–6141	$14^h 13^m 10^s$	$-61°41'13''$	0.2856	333.44	13.6	677	10.1	56.5

2.3 Other observations

We have used several other data sets in this study.

(i) Radio data from the MOST at 843 MHz (Green et al. 1999).

(ii) Single-dish continuum and H I data for this region, at 21 cm, which were taken as part of the Southern Galactic Plane Survey (McClure-Griffiths et al. 2001).

(iii) Images from the Cohen & Green (2001) study of this region of the Galactic plane in the mid-infrared using observations made with the *Mid-course Space Experiment* (*MSX*).

3 RADIO DATA REDUCTION

Reduction and analysis of the radio data were carried out with the MIRIAD package using standard techniques described in *The Miriad User's Guide* (Sault & Killeen 1998). The primary calibrator PKS B1934–638 was used for flux density and bandpass calibration. The secondary calibrator B1329–665 was used to solve for antenna gains, phases and polarization leakage terms. After calibration was completed, the continuum data were recorded as 13 channels each with 8-MHz bandwidth. The spectral line data have 512 channels, each with a velocity resolution of 1.6 km s^{-1}.

3.1 Continuum image

The continuum data were reduced using mosaicking techniques in order to account for the two different pointing centres. The image was formed using a weighting scheme intermediate between natural weighting (which minimizes noise) and uniform weighting (which minimizes sidelobe levels). This was achieved by setting the ROBUST

parameter to 0.5 in the INVERT task, giving nearly the same sensitivity as natural weighting but with significantly lower sidelobes. The image was deconvolved using a maximum-entropy algorithm, which is implemented in the task MOSMEM (Sault, Staveley-Smith & Brouw 1996). The final image has 3-arcsec pixels and a beamsize of 25 arcsec. The rms noise in the image is 0.5 mJy beam^{-1}, which is higher than the theoretical value but not unexpected considering the excess background emission in the Galactic plane. This image is shown in Fig. 2.

A second image was also formed, combining the ATCA interferometric data with single-dish data from the Parkes radio telescope (McClure-Griffiths et al. 2001). There are two possible methods for doing this. One is a non-linear technique whereby the data are combined in the *uv*-plane and then jointly deconvolved. An alternate method, which is used here, combines the data in the Fourier domain after both have been separately deconvolved (e.g. McClure-Griffiths et al. 2001). This was implemented by the task IMMERGE in MIRIAD. Including the single-dish data adds the smoothly varying component of the source and the diffuse Galactic emission.

Finally, a high-resolution image was produced, with 6-arcsec resolution, using only the baselines with the 6-km antenna. This resolves out most of the extended emission and allows better sensitivity for point sources hidden beneath the extended structure. The rms noise in this image is 0.07 mJy beam^{-1}.

3.2 Polarization images

Stokes *Q*, *U* and *V* images were formed by inverting and cleaning each of the 13 frequency channels separately, using the task
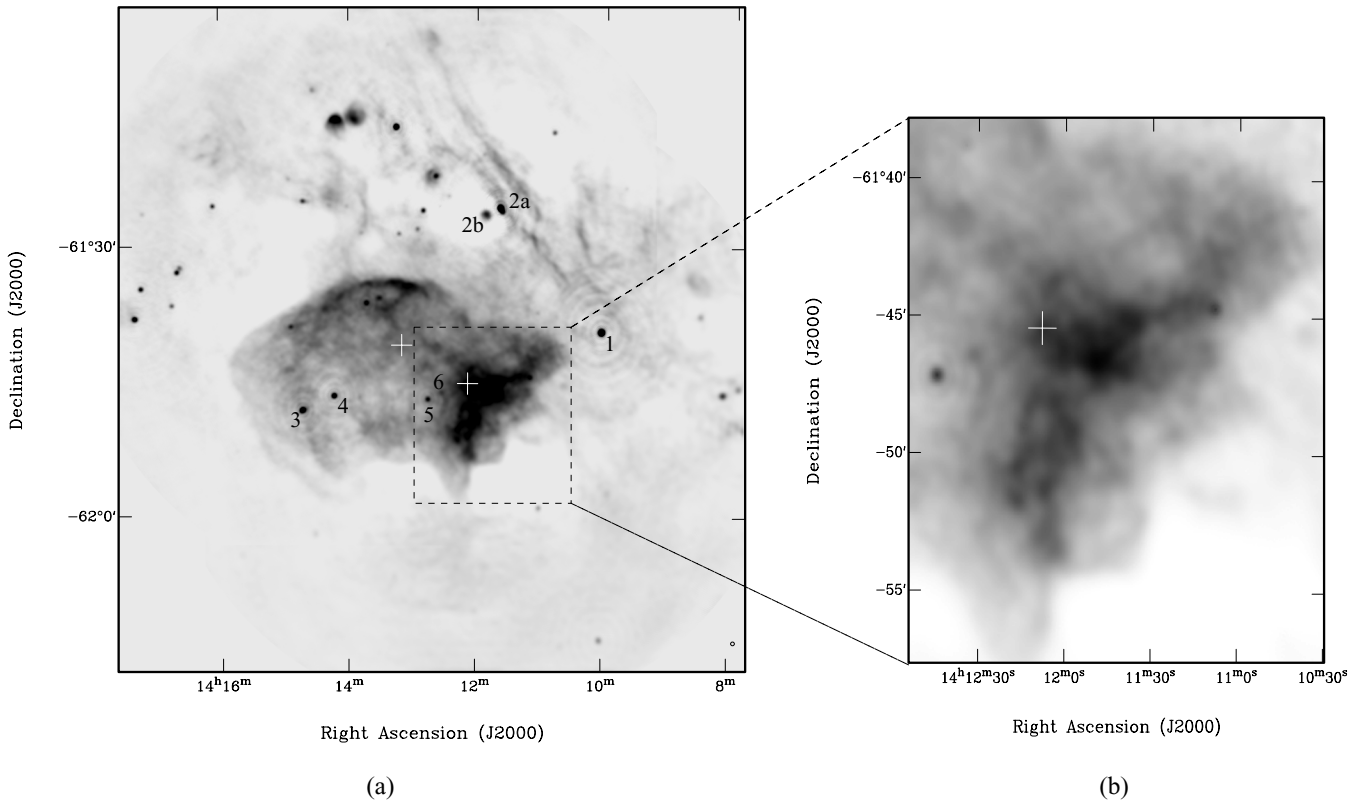
Figure 2. ATCA grey-scale images of SNR G312.4–0.4 at 1384 MHz. The images have a resolution of 25 arcsec. The grey-scale range of image (a) is 0–20 mJy beam^{-1} and that of image (b) is 0–30 mJy beam^{-1}. The FWHM of the restoring beam is shown in the lower corner of each image. The positions of PSRs J1413–6141 and J1412–6145 are marked with white crosses and seven unresolved sources have been labelled as objects of interest as possible counterparts to the EGRET source. The western region of the SNR, part of which may be a PWN, has been enlarged to show more detail.
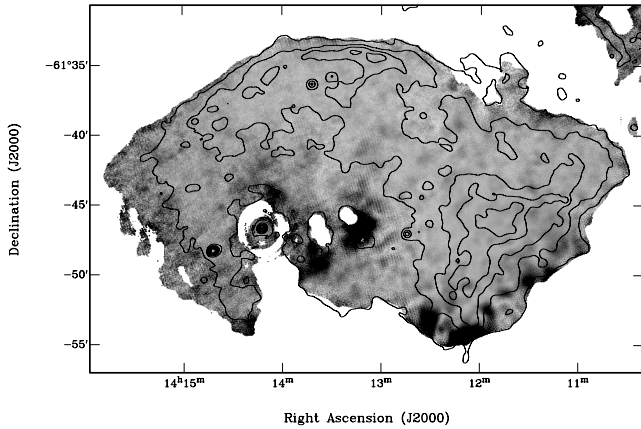
Figure 3. Fractional polarization for SNR G312.4–0.4 at 1384 MHz. The grey-scale ranges from 0 per cent (white) to 7 per cent (black). Contours show the radio continuum and the levels are 5, 10, 15, 20, 25, 30, 40 mJy beam^{-1}.

PMOSMEM. A linear polarization image, L, was formed for each channel from the final Q and U images, where $L = \sqrt{Q^2 + U^2}$. The position angle image, PA, was also calculated, where PA $= \frac{1}{2}\tan^{-1}(U/Q)$. The L images were then summed over all channels to produce a final linear polarization image and a bias was removed to ensure the noise in the image had zero mean. The final rms noise of this image is 0.14 mJy beam^{-1}, significantly better than for the total intensity. The resulting polarization image was divided by the total intensity image and clipped where the total intensity emission was less than 5σ (2.5 mJy beam^{-1}), to form a fractional polarization image. This is shown in Fig. 3.

3.3 Spectral index

In order to compute spectral indices using data from only two wavelengths, it is essential that the flux densities be accurately determined. For an interferometer, the integrated flux density measured depends on the length of the shortest baseline used, in other words, the largest spatial scale that is detected. It is, therefore, important that the data contain the same spatial scales (e.g. Gaensler et al. 1999; Katz-Stone et al. 2000).

To match the ATCA and MOST data, we created a new continuum image at 20 cm, using only the pointing centred at RA (J2000) $14^h\ 12^m\ 00^s$, Dec. (J2000) $-61°47'30''$. These data contain baselines of $\leqslant$750 m and have a similar beam ($\sim$40 arcsec) to the MOST image at 843 MHz. The two images still have different uv coverage, so spatial filtering was carried out to equalize the spatial content of the two images. Extended structure was excluded from the 843-MHz image and the 1384-MHz image was smoothed to the lower resolution of the 843-MHz image.

We used two methods for calculating spectral indices, spectral tomography and temperature–temperature (T–T) plots and the results were compared, for consistency. Spectral tomography produces maps of the following quantity:

$$I_t(\alpha_t) = I_1 - \left(\frac{\nu_1}{\nu_2}\right)^{\alpha_t} I_2, \qquad (1)$$

where α_t is the spectral index, as defined by $S_\nu \propto \nu^\alpha$, and I_1 and I_2 are the intensities of a given pixel at ν_1 (843 MHz) and ν_2 (1384 MHz), respectively (Katz-Stone et al. 2000). A series of maps was made for $-1.0 \leqslant \alpha_t \leqslant 0.1$ in steps of 0.1. Any regions

of the image that vanish into the background have $I_t(\alpha_t) = 0$ and a spectral index of α_t.

T–T plots traditionally involve plotting the brightness temperature of two images against each other, pixel-by-pixel. However, the flux density in units of Jy beam^{-1} can be used providing the two images have the same beam size (Bock 1997). This method is independent of any zero error, and the slope of the line of best fit is given by

$$m = \left(\frac{\nu_1}{\nu_2}\right)^{\alpha}, \qquad (2)$$

where α is the spectral index. The uncertainty in the linear fit may be underestimated as adjacent pixels are not independent and there are typically many pixels per beam. This effect can be corrected for by rebinning each image, taking every ith pixel where there are i pixels beam^{-1} in each dimension (Gaensler et al. 1999). T–T plots were made for subsets of the images at the northern rim of the SNR and also at the brightest part of the western region. A linear least-squares fit was then used to determine the slope for each region. The results were checked for self-consistency by varying the box size for the plots (i.e. the number of pixels) and by shifting the box by a few pixels. The slope stayed the same for each respective region and the fit improved with the inclusion of more pixels.

3.4 Spectral line

After flagging and calibration of the two H I data sets, we performed continuum subtraction (task UVLIN) by fitting a second-order polynomial to the line-free channels. A 'dirty' cube was produced using the task INVERT, selecting only those baselines that were longer than 125 m and using uniform weighting. The output cube consists of 150 channels each 2 km s^{-1} wide starting at -120 km s^{-1}. The cube was not cleaned but was convolved with a Gaussian restoring beam of size 45 arcsec.

We made a continuum image in an identical fashion using the two data sets and the same parameters in INVERT. In this case we cleaned the image appropriately and restored it with the same Gaussian beam of FWHM 45 arcsec.

The rms noise as a function of channel number was computed using the routine IMSTAT. The sensitivity varies over the bandpass depending on the temperature of the H I emission in a given channel. Although the presence of variable sky structure in the cube will adversely affect the computed rms noise, this was the best way to assess the significance of any detected absorption feature. The data were then scaled by the total flux in the continuum image. This allows the fractional absorption depth to be computed and the significance of the feature to be estimated.

An emission profile was obtained using the Parkes single-dish data, for a location just outside the SNR McClure-Griffiths et al. (2001).

4 RESULTS

4.1 Continuum image

Radio continuum images of SNR G312.4–0.4 with a resolution of 25 arcsec and an rms noise of 0.5 mJy beam^{-1} are shown in Fig. 2. The SNR is seen as an incomplete shell, with a horseshoe-like appearance. Its brightest regions are the extended western component and the north rim. The arc-shaped blow-out feature that is visible in the MOST image to the south of the SNR can only be seen very faintly here, because of partial primary beam correction. The brightest part of the western region of the SNR has a flux density of

~30 mJy beam^{-1}. It extends over a region of 14×7 arcmin^2 and has an integrated flux density of ~5 Jy, with the contribution from the shell subtracted. The morphology of the western bright region consists of a complicated filamentary structure, which is seen for the first time. The brightest parts of the northern rim of the SNR have flux densities of ~20 mJy beam^{-1}.

There are several bright, unresolved sources in the image. Seven of the sources (labelled in Fig. 2) are now discussed. Source 1 (G312.11–0.2) is non-thermal with a flux density of 600 mJy at 408 MHz (Caswell & Barnes 1985) and 166 ± 3 mJy at 1384 MHz. It is classified as extragalactic by (Cohen & Green 2001). Source 2a (G312.36–0.04) has a flux density of 173 ± 6 mJy at 1384 MHz and is classified as a compact H II region (Cohen & Green 2001), but the nature of source 2b (flux density 75 ± 2 mJy at 1384 MHz) is unclear although it is probably non-thermal. The flux densities at 408 MHz and 5 GHz given by Caswell & Barnes (1985) are affected by blending between the two sources. Sources 3–6 have 1384-MHz flux densities of 74 ± 6, 59 ± 6, 35 ± 7 and 17 ± 8 mJy, respectively. These sources lie within the SNR shell and confusion with the underlying SNR emission contributes to the large error bars. Source 5 is seen in the infrared and although not classified by Cohen & Green (2001) is thought to be a compact H II region. Source 6 has an X-ray and an infrared counterpart and is thus likely to be stellar.

The two pulsars listed in Table 1 are not visible in Fig. 2 but their positions are shown as crosses. They are detected in the high-resolution image and our positions agree, within the uncertainties, with those from the Parkes Multibeam Survey (Manchester et al. 2001). We measured flux densities at 1384 MHz of 0.79 ± 0.07 and 0.73 ± 0.07 mJy for PSRs J1413–6141 and J1412–6145, respectively.

The long filaments to the north-west of the SNR have a flux density of ~20 mJy beam^{-1} and are also visible in the infrared (see Section 4.5).

There are several weak background sources in the image that are almost certainly extragalactic. These are unlikely to be responsible for the γ-ray emission as their flux density is a factor $\gtrsim 100$ weaker than the known EGRET blazars (Mattox et al. 1997).

4.2 Polarization

The fractional polarization image is shown in Fig. 3. The image has been masked where the total intensity is less than 2.5 mJy beam^{-1}. The strongest polarization comes from a small area at the southern tip of the western region of the SNR, which is polarized at around 5–10 per cent. It is offset by approximately 1 arcmin from a bright spot in the radio continuum. This is an unusual feature, the origin of which is unclear.

The absence of any significant polarization at 1384 MHz is somewhat surprising, particularly as the western edge of the SNR is polarized at the 20 per cent level at 8.5 GHz (Whiteoak 1993). The lack of polarization at 1384 MHz can possibly be explained by beam depolarization, resulting from changes in the degree of foreground Faraday rotation on scales smaller than the synthesized beam. Regions of significant beam depolarization at this frequency have indeed been determined for nearby regions of the Galactic plane (Gaensler et al. 2001).

4.3 Spectral indices

T–T plots were made for the western part of the SNR shell and the northern rim and the results are shown in Fig. 4. As described in Section 3.3, only independent pixels have been used, in order to
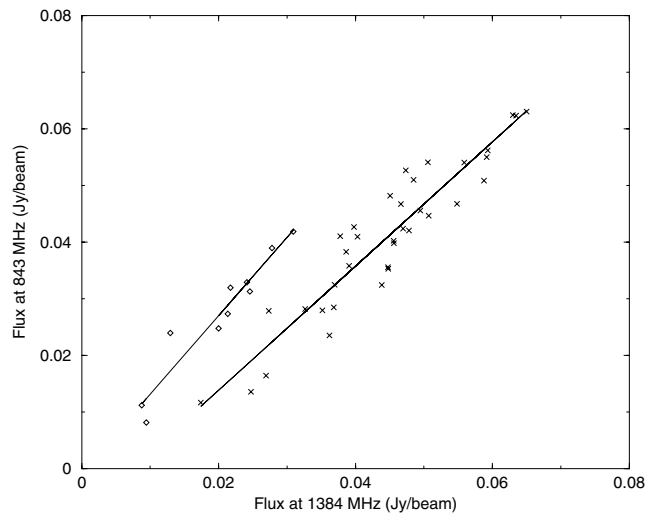

Figure 4. T–T plots for two subregions of SNR G312.4–0.4. The diamonds show points from the northern rim, whereas the crosses show points in the western region. The slope of the best-fitting line to the distribution from the rim is 1.4 ± 0.14, giving $\alpha = -0.7 \pm 0.1$ and the slope of the best-fitting line to the points from the western region is 1.1 ± 0.07, giving $\alpha = -0.19 \pm 0.01$.

avoid underestimating the uncertainties. The two regions have significantly different spectral indices. The slope of the linear fit for each region is related to the spectral index as expressed in equation (2). The slope of the distribution of points along the rim gives $\alpha = -0.7 \pm 0.1$, which is typical of synchrotron radiation seen from shell SNRs. The distribution of points from the western region gives $\alpha = -0.19 \pm 0.01$. This value is much flatter than the typical spectral indices for shell SNRs ($-0.4 \lesssim \alpha \gtrsim -0.7$) but lies well within the typical range expected for a PWN ($0.0 \lesssim \alpha \gtrsim -0.3$).

Spectral tomography indicates a spectral index of between -0.6 and -0.8 for the northern rim and a value that is much flatter for the western region, consistent with the T–T result.

4.4 X-rays

There are no bright sources in the X-ray image. An application of WAVDETECT to the 0.2–8 keV data using a threshold SN = 2 detected only 18 sources. Several of these were identified with bright stars; none correlate with the bright radio point sources. Presumably, most of these sources are coronal emission from field stars or (for a few hard absorbed sources) emission from background active galactic nuclei. Any emission from the G312.4–0.4 complex should also be highly absorbed. We therefore formed a 2–8 keV image and replaced the counts from the apertures of all point sources detected in the full-band image with Poisson counts from the local 2–8 keV background. The background counts pixel^{-1} were generally quite constant across the frontside illuminated chips. We subtracted the average counts pixel^{-1} from chips I0–I3 and S2 and a separate background from the back-illuminated S3 chip. No exposure correction was applied as the fluctuations at the chip boundaries obscured any potential diffuse emission. After binning and adaptive smoothing, the resultant ACIS image is plotted in Fig. 5 with the 20-cm radio contours overlaid. A few regions of excess emission are seen, but at the western limb of the SNR only a slight excess in the diffuse hard count rate is visible. No significant diffuse emission is seen below 2 keV, indicative of high absorption.
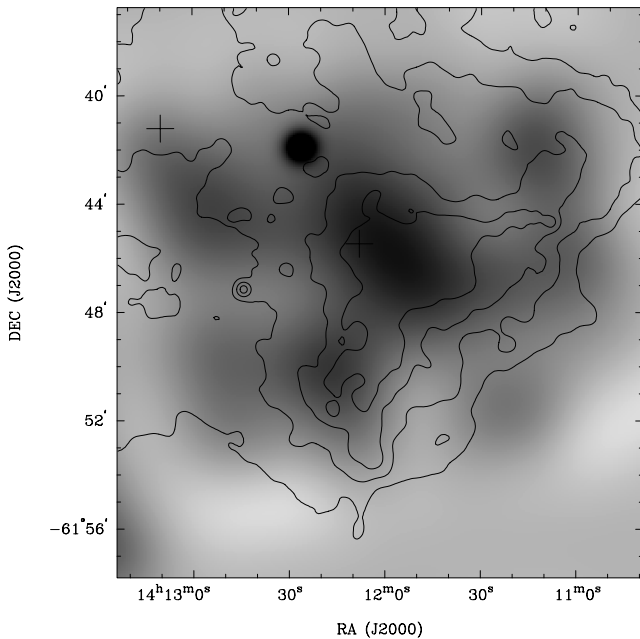
Figure 5. Smoothed ACIS-I+S2/S3 (2–8 keV) image of unresolved emission in the direction of G312.4–0.4. The radio contours and pulsar positions (crosses) are shown. Point source subtraction was carried out and the nature of the remaining source is unknown. Only the region with clear structure is significant. The edges of the image are outside the chip coverage.

This diffuse X-ray emission from the western region is marginally detected. In the (unsmoothed) 2–10 keV point source-removed image, we find 105 ± 24 excess counts in a 6×6 arcmin^2 region covering the brightest portion of the radio image. For typical $\langle n_{\mathrm{HI}}/n_{\mathrm{e}} \rangle$ values of 10–30, the dispersion measure inferred H I column density to PSR J1412–6145 is comparable to or greater than the total column of Galactic gas in this general direction, $N_{\mathrm{H}} = 2.2 \times 10^{22}$ cm^{-2} (Dickey & Lockman 1990). Adopting this latter column density and assuming a power-law distribution with an index of $\Gamma = 1.5$, which is generic for the hard component of young pulsars and their nebulae, we calculate a flux in X-rays of f_{X} (2–8 keV) $= 3.2 \pm 0.7 \times 10^{-13}$ erg cm^{-2} s^{-1}. This flux value is fairly insensitive to N_{H} unless it substantially exceeds 10^{23} cm^{-2}. The *ASCA* archival images also show some hard X-rays associated with this diffuse source. There is enhanced emission in the range 4–10 keV that has a flux of $\sim 4.5 \times 10^{-13}$ erg cm^{-2} s^{-1}. This is consistent with the *Chandra* results.

We have also looked for unresolved sources corresponding to PSR J1412–6145 and J1413–6141. No counts are detected at either position. PSR J1412−6145 is close to the optical axis of the ACIS-I and the excellent point spread function allows us to put an upper limit on the counts (2–8 keV), assuming an unabsorbed energy distribution with a power-law index $\Gamma = 1.5$, which is equivalent to a flux of 6×10^{-15} erg cm^{-2} s^{-1} (3σ). At the position of PSR J1413–6141, the degraded point spread function allows an upper limit of 1.8×10^{-14} erg cm^{-2} s^{-1}(3σ), insensitive to a moderate range of N_{H} values.

4.5 Infrared

Fig. 6 shows radio contours overlaid on the mid-infrared 8-μm image from the *MSX* satellite (Cohen & Green 2001). A very striking feature of Fig. 6 is the presence of thermal and radio continuum
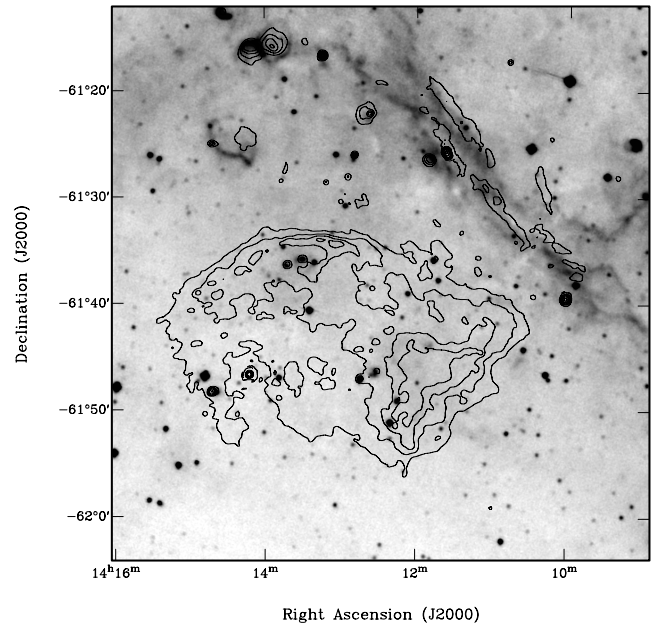
Figure 6. 8-μm mid-infrared image with 6-arcsec pixels, overlaid with radio contours at 20 cm. The grey-scale ranges from 0.78 MJy sr^{-1} to 10 MJy sr^{-1}. Contour levels are 5, 10, 15, 20, 30, 50, 90 and 120 mJy beam^{-1}.

filaments running diagonally across the image. The bright filaments in the infrared are slightly offset from those in the radio. Cohen & Green (2001) have made an extensive comparison of this region in the radio and the infrared. They discuss the nature of the filaments (and other sources) in detail.

Although there is some diffuse infrared emission throughout the SNR it is clear that there are no major H II regions within its boundaries. In particular, the western part of the shell, which has a flat spectral index in the radio, is not an obvious thermal source. As previously mentioned, radio sources 5 and 6 have infrared counterparts and there is also a cluster of strong infrared sources close to the top rim of the SNR that are likely to be H II regions or stars.

4.6 H I spectral line data

We compare our resulting absorption spectra with the emission profile in that direction, obtained from the Parkes data (McClure-Griffiths et al. 2001). Fig. 7 shows the emission profile and directly underneath it, the absorption spectra for Source 1 (as marked in the continuum image in Fig. 2). The brightness temperature is scaled to match the value in the (Kerr et al. 1986) H I emission survey of this part of the Galaxy. The dashed line is the 1σ envelope, plotted as a function of velocity channel and clearly shows that the noise in the line is approximately four to five times higher than the rms noise off-line. Below the spectra we show the rotation curve appropriate for this longitude. To compute the rotation curve we use an analytic expression given by the best-fitting model of the Galactic rotation curve from Fich, Blitz & Stark (1989). We adopt the standard IAU parameters (Kerr & Lynden-Bell 1986) for the distance to the Galactic Centre ($R_0 = 8.5$ kpc) and the solar orbital velocity ($V_0 = 220$ km s^{-1}). The rotation curve of the Galaxy is the azimuthally smoothed average of its velocity field and thus implicitly assumes circular orbits around the Galactic Centre.

The emission spectrum is somewhat unusual in that it shows relatively weak emission at zero velocity. High brightness temperature
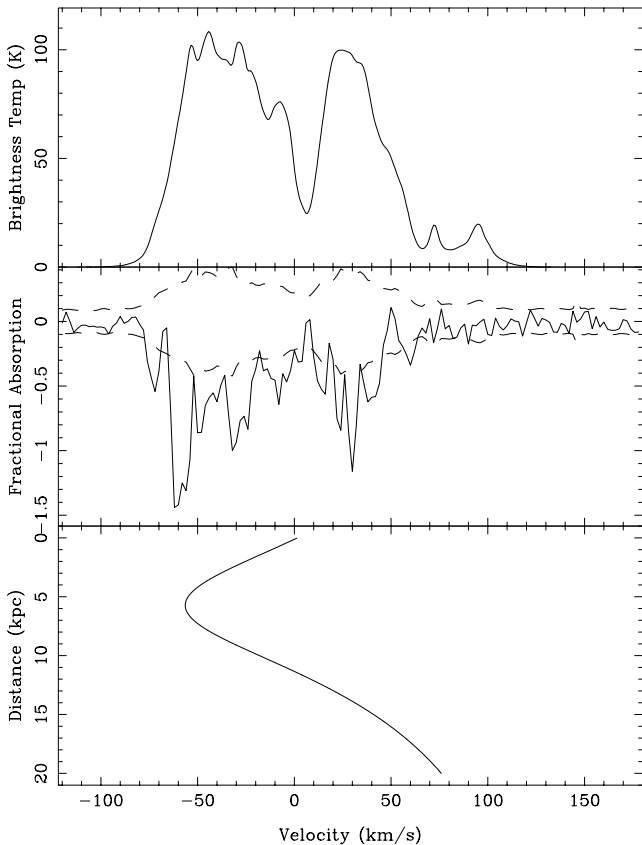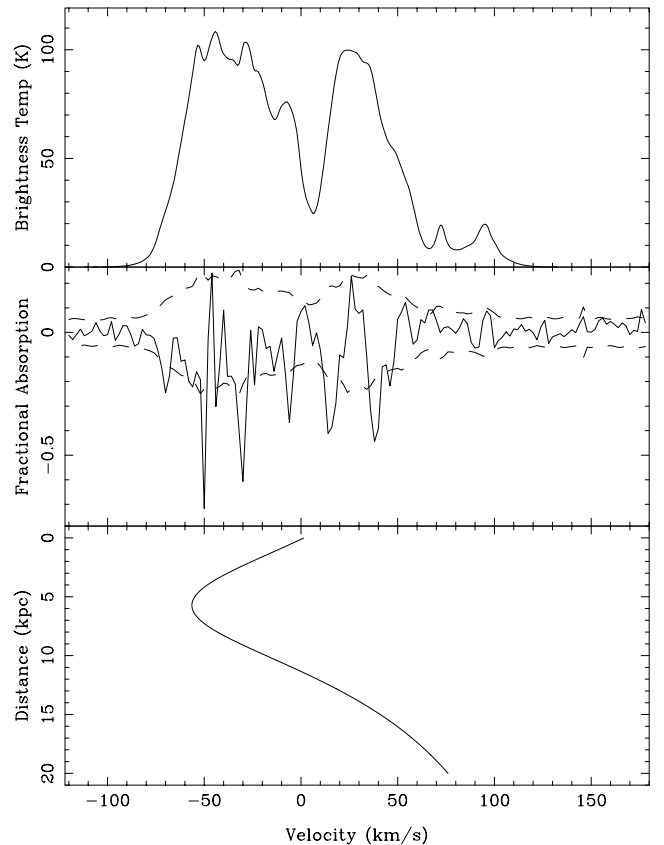
Figure 7. Emission (top) and absorption (middle) spectra in the direction of the point source P1. The dashed line in the middle panel shows the 1σ envelope as a function of velocity channel. The bottom panel shows the conversion of velocity to distance at this Galactic longitude.

Figure 8. Emission (top) and absorption (middle) spectra in the direction of the western part of the SNR. The dashed line in the middle panel shows the 1σ envelope as a function of velocity channel. The bottom panel shows the conversion of velocity to distance at this Galactic longitude.

gas is seen out to the tangent point at -55 km s^{-1}. At positive velocities we see 100 K gas out to $+40$ km s^{-1} and two further weak emission features at $+70$ and $+95$ km s^{-1}. One would not expect to see absorption against these two weak features.

The absorption spectrum for Source 1 (Fig. 7) displays deep absorption at all negative velocities out to the tangent point. Absorption with a similar optical depth to the negative velocity features is also seen from $+20$ to $+50$ km s^{-1}. Source 1 shows absorption against all the main emission features and it is almost certainly extragalactic, confirming the classification of Cohen & Green (2001). The absorption spectrum for Source 2a is very similar to that of Source 1 and it seems probable that it is also extragalactic. This is at odds with the compact H II region classification of Cohen & Green (2001), but it is likely that their infrared-to-radio flux ratio (on which their classification is based) is too high because of confusion with the (foreground) filamentary structure. None of the other point sources were of sufficient flux density to show significant absorption in their spectra.

Fig. 8 shows the absorption spectrum in the direction of the western region of the SNR. The spectrum exhibits deep absorption features at negative velocities out to the tangent point. Features with a smaller optical depth are also seen, at $+20$ and $+40$ km s^{-1}, with a significance of 4σ. Given the deeper absorption features out to the tangent point, we can certainly impose a lower distance limit of 6 kpc. Any conclusions beyond this then depend on the interpretation of the features at $+20$ and $+40$ km s^{-1}. If

these absorption features are real, a lower distance limit of 14 kpc is implied.

The absorption spectrum towards the northern rim is very noisy and cannot provide any direct evidence of whether or not the northern rim and the western region are physically connected.

5 DISCUSSION

Given the uncertainties in the interpretation of the absorption spectrum, in the following discussions we adopt a distance of $6d_6$ kpc to the SNR complex.

5.1 Origin of the SNR

As the main shell is quite symmetrical, we estimate its centre to be at RA (J2000) $14^h 13^m 00^s$, Dec. (J2000) $-61°43'00''$. The radius of the shell is then 13 arcmin, equivalent to a physical radius of $23d_6$ pc. Assuming an ambient density of $n \sim 1$ cm^{-3}, the mass swept up by the shell is $\sim 1200\, d_6^3$ M$_\odot$. This implies that the SNR is well into the Sedov–Taylor (adiabatic) phase of expansion as it has swept up more than 20 times the mass ejected (Dohm-Palmer & Jones 1996).

We can relate the initial conditions of the SN to the radius of the expanding shock front by

$$R(t) = 5.39 \left(\frac{E_{51} t^2}{n} \right)^{0.2} \text{pc}, \tag{3}$$

where E_{51} is the kinetic energy of the explosion in units of 10^{51} erg, t is the time after the explosion in kyr and n is the density of the medium into which the SNR is expanding in particles cm^{-3}. Assuming that the age of the SNR is the same as PSR J1412–6145 (50 kyr), we find the ratio $E_{51}/n \sim 0.6\, d_6^5$. Alternatively, the age of PSR J1413–6141 (13 kyr), yields a ratio of $E_{51}/n \sim 9\, d_6^5$. Given the uncertainties of the pulsar ages and the SNR distance, both these values are well within expected bounds for the adopted distance, $d = 6$ kpc. However, if $d \geqslant 14$ kpc then PSR J1413–6141 may be ruled out as the progenitor star for the SN explosion, as E_{51}/n becomes unreasonably large.

The pulsar velocities can be calculated by assuming, in turn, that each was the progenitor star for the SNR. This implies a transverse velocity of $v = 218 d_6$ km s^{-1} for PSR J1412–6145 and $v = 288 d_6$ km s^{-1} for PSR J1413–6141. Again, both of these values are entirely consistent with pulsar velocities in general (Cordes & Chernoff 1998), even if $d \geqslant 14$ kpc.

5.2 A PWN around PSR J1413–6141?

We might expect to see a radio PWN surrounding PSR J1413–6141, a young, highly energetic pulsar. Gaensler et al. (2000) discuss two types of PWN that can form a static PWN, which is confined by the gas pressure of the surrounding interstellar medium and a bow-shock PWN confined by ram pressure from the motion of the pulsar through the medium. The condition for a static PWN is given by

$$nV^5 \leqslant 4 \times 10^9 \dot{E}_{34}/t^2, \tag{4}$$

where V is the pulsar velocity in km s^{-1}, $\dot{E}_{34}$ is the spin-down energy in units of 10^{34} erg s^{-1} and the other symbols are as defined earlier. Taking a lower limit on n of 0.003 cm^{-3}, the velocity of the pulsar would need to be less than 210 km s^{-1} for this condition to be met. If this is the case, the size of the static PWN can be computed via

$$R_{\text{static}} = 0.14 \left(\frac{\dot{E}_{34} t^3}{n} \right)^{0.2} \text{pc} \tag{5}$$

yielding a radius of 4.8 pc. This PWN would be resolved in our image for any sensible pulsar distance but distinguishing the PWN from the remaining SNR structure is virtually impossible.

If the pulsar velocity is in excess of 210 km s^{-1}, it will have overtaken its static PWN, resulting in a bow-shock PWN with a characteristic scale size of

$$R_{\text{bow-shock}} = 0.63 \left(\frac{\dot{E}_{34}}{nV^2} \right)^{1/2} \text{pc}. \tag{6}$$

Even for a lower limit on n of 0.003 cm^{-3}, the bow shock PWN would be unresolved in our image. Assuming a typical PWN spectral index $\alpha = -0.3$ and integrating from 10 MHz to 100 GHz, if the PWN is unresolved then the efficiency of the pulsar is given by

$$\epsilon = 4.8 \times 10^{-6} \frac{d^2 S_{1.4}}{\dot{E}_{34}}, \tag{7}$$

where $S_{1.4}$ is the PWN flux density at 1384 MHz in mJy. In our case we measure a flux density of 0.97 mJy at the pulsar position as compared with a catalogue value of 0.51 mJy for the pulsed flux. Generously assuming a PWN flux of 0.5 mJy the efficiency is then $\leqslant 1.5 \times 10^{-6} d_6^2$. This is more than an order of magnitude less than expected for pulsars of this age (Gaensler et al. 2000).

We therefore conclude that PSR J1413–6141 has a velocity less than 200 km s^{-1} and has formed a static PWN the surface brightness of which is confused with other emission or below our detection limit. This again points to the fact that PSR J1413–6141 is likely not to be associated with the SNR.

5.3 Evidence for a PWN near PSR J1412–6145?

There is circumstantial evidence that the western part of the SNR is a PWN. Whiteoak (1993) reports 20 per cent polarization at 8 GHz and, as we have derived, the spectral index of this region is rather flat. However, the lack of polarization at both 5 and 1.4 GHz is puzzling. This either implies a substantial rotation measure or that the 8-GHz polarization is overestimated. On the other hand, if this *is* a PWN we need to determine the nature of its power source.

The integrated flux density of the PWN is $\sim$5 Jy. Using the measured spectral index of -0.2, we estimate the integrated radio luminosity from 100 MHz to 100 GHz to be $\sim 1.1 \times 10^{34} d_6^2$ erg s^{-1}. The PWN covers an area of $12 \times 24\, d_6^2$ pc and so we assume a value of $\sim$9 pc for its radius in the subsequent discussion. We can relate the radio luminosity, L_R, of a PWN to the spin-down energy of the central source via $L_R = \epsilon \dot{E}$, where ϵ is the efficiency. Gaensler et al. (2000) showed that in young pulsars ϵ was of the order of 10^{-4}, and hence one requires the central pulsar to have $\dot{E} \gtrsim 10^{38} d_6^2$ erg s^{-1} in our case. A pulsar of this $\dot{E}$ should be highly visible in the X-ray range. Furthermore, the two known pulsars in the field have $\dot{E} \sim 10^{35}$ erg s^{-1}, which is clearly not high enough to power a PWN of such a size and luminosity. The lack of any obvious high-$\dot{E}$ pulsar in the *Chandra* image, and the low values of $\dot{E}$ for the known pulsars are inconsistent with the calculated parameters for a PWN. If $d \sim 14$ kpc, then both L_R and the size of the region become improbably large for a PWN. The source of the electrons powering this radio enhancement remains unclear.

5.4 X-ray emission

The limits on the X-ray luminosity of PSRs J1412–6145 and J1413–6141 are 2.6×10^{31} and 7.8×10^{31} erg s^{-1}, respectively, assuming a distance of 6 kpc. This implies an X-ray efficiency of less than 2.1×10^{-4} and 1.4×10^{-4}. These limits are similar to the expected values for these sources from the Possenti et al. (2002) relation and are also in line with other pulsars of similar ages, e.g. the Vela pulsar and the recently discovered pulsar PSR J2229+6114 (Halpern et al. 2001).

The X-ray luminosity of the diffuse emission near PSR J1412–6145 is 1.4×10^{33} erg s^{-1}. This is comparable to the luminosity of the diffuse nebula surrounding PSR B1951+32 in CTB 80, although the $\dot{E}$ of this pulsar is higher than that of PSR J1412–6145 by a factor of $\sim$30 (Safi-Harb, Ogelman & Finley 1995). Therefore, the weak diffuse X-ray emission seen from this region in the *ASCA* and CXO data could plausibly be a PSR J1412–6145 powered PWN.

5.5 γ-ray emission

The third EGRET catalogue (Hartman et al. 1999) gives the integrated flux of the γ-ray source as $F = 64.2 \times 10^{-8}$ photon cm^{-2} s^{-1} with a photon index of 2.12. Using an upper cut-off of 10 GeV, this gives a γ-ray luminosity, $L_\gamma = 2.1 \times 10^{36} d_6^2$ erg s^{-1}, assuming isotropic radiation or $1.7 \times 10^{35} d_6^2$ erg s^{-1} into 1 sr. Tompkins (1999) has computed a variability index for the EGRET sources, finding a value of $0.33^{+0.22}_{-0.17}$ for 3EG J1410–6147. Nolan et al. (in preparation) using a revised statistic similarly find the value $0.32^{+0.32}_{-0.24}$. These results show only that the source is significantly less variable than the bright EGRET blazars, suggesting a pulsar or diffuse emission source of γ-ray flux.

The latter value of $L_\gamma = 1.7 \times 10^{35} d_6^2$ erg s^{-1} is 139 per cent of the $\dot{E}$ for PSR J1412–6145 and 30 per cent of the $\dot{E}$ for PSR J1413–6141, even at $d = 6$ kpc. Generally, one observes an increasing

efficiency with decreasing $\dot{E}$ and PSR B1055–52 is the most efficient γ-ray pulsar with efficiency of 15 per cent (Thompson 1998) and $\dot{E}$ is a factor of 10 lower than PSR J1413–6141. For PSR J1412–6145 to be the γ-ray source, a small beaming angle and a high efficiency would need to be invoked. The efficiency of PSR J1413–6141 is an order of magnitude higher than expected for its $\dot{E}$ and therefore it is unlikely that either pulsar powers the γ-ray source unless the distance is substantially smaller than that inferred from dispersion and H I measurements.

With the existence of a PWN uncertain and prima facie evidence for γ-ray emission from the pulsars unconvincing, the origin of the γ-ray source 3EG J1410–6147 remains a mystery. It is tempting to speculate on the existence of a third young pulsar in this region. It would have $\dot{E} \sim 10^{37}$ erg s^{-1}, sufficient to explain the γ-rays and power the radio PWN. The main problem with this explanation is that its X-ray efficiency would have to be extremely low ($\leqslant 10^{-6}$) to explain its non-detection in our X-ray observations. It would then have the lowest value, by an order of magnitude, of L_x/L_γ of any of the known pulsars. A plausible alternative model could be based on the interaction of the western edge of the SNR with a nearby molecular cloud (e.g. Aharonian, Drury & Voelk 1994) and Esposito et al. (1996).

6 CONCLUSIONS

We have made a continuum image of the SNR G312.4–0.4 and surrounding regions at 1384 MHz, with a resolution of 25 arcsec. We also made observations in the 21-cm H I line and produced absorption spectra to obtain a lower distance limit to the SNR of 6 kpc. If absorption features at positive velocities are real, the SNR is located beyond 14 kpc. Although the bright, western portion of the SNR resembles a PWN, at these distances PSR J1412–6145 seems inadequate to power the observed enhancement to the radio flux. The lack of a radio PWN around the 13-kyr PSR J1413–6141 indicates that it is likely to be slow moving and hence not formed with SNR G312.4–0.4. We suggest that the 50-kyr pulsar, PSR J1412–6145, originated in the same explosion as the SNR.

The two young pulsars superimposed on the SNR are not detected in the X-rays, although the implied 10^{-4} limits on the X-ray efficiencies are not strongly constraining. Neither of these two pulsars can account for the γ-ray luminosity unless abnormally high efficiency, small beaming angle and a low distance are invoked.

The most likely interpretation of the multiwavelength data of this region is (i) the SNR is large, old ($\sim$50 000 yr) and distant, with PSR J1412–6145 as the likely progenitor; (ii) the bright western region of the SNR is most probably an amorphous, flat spectrum part of the SN shell; and (iii) the γ-rays are unrelated to the SNR.

The γ-ray source 3EG J1410–6147 still remains unidentified. The launch of the *Gamma-ray Large Area Space Telescope* in 2005 will reduce the size of the positional error box to 1 arcmin and provide a resolution to this puzzle.

ACKNOWLEDGMENTS

REFERENCES

Aharonian F., Drury L., Voelk H., 1994, A&A, 285, 645
Bock D., 1997, PhD thesis, Univ. Sydney
Case G., Bhattacharya D., 1999, ApJ, 521, 246
Caswell J., Barnes P., 1985, MNRAS, 216, 753
Cohen M., Green A.J., 2001, MNRAS, 325, 531
Cordes J.M., Chernoff D.F., 1998, ApJ, 505, 315
Cordes J., Lazio T., 2002, preprint (astro-ph/0207156)
Dickey J.M., Lockman F.J., 1990, ARA&A, 28, 215
Dohm-Palmer R.C., Jones T.W., 1996, ApJ, 471, 279
Esposito J.A., Hunter S.D., Kanbach G., Sreekumar P., 1996, ApJ, 461, 820
Fich M., Blitz L., Stark A.A., 1989, ApJ, 342, 272
Frater R.H., Brooks J.W., Whiteoak J.B., 1992, J. Electr. Electron. Eng. Aust., 12, 103
Gaensler B.M., Brazier K.T.S., Manchester R.N., Johnston S., Green A.J., 1999, MNRAS, 305, 724
Gaensler B., Stappers B., Frail D., Moffett D., Johnston S., Chatterjee S., 2000, MNRAS, 318, 58
Gaensler B., Dickey J., McClure-Griffiths N., Green A., Wieringa M., Haynes R., 2001, ApJ, 549, 959
Green A.J., Cram L.E., Large M.I., Ye T.-S., 1999, ApJS, 122, 207
Halpern J.P., Camilo F., Gotthelf E.V., Helfand D.J., Kramer M., Lyne A.G., Leighly K.M., Eracleous M., 2001, ApJ, 552, L125
Hartman R.C. et al., 1999, ApJS, 123, 79
Johnston S., Koribalski B., Weisberg J.M., Wilson W., 2001, MNRAS, 322, 715
Katz-Stone D., Kassim N., Lazio T., O'Donnell R., 2000, ApJ, 529, 453
Kerr F.J., Lynden-Bell D., 1986, MNRAS, 221, 1023
Kerr F.J., Bowers P.F., Jackson P.D., Kerr M., 1986, A&AS, 66, 373
Manchester R.N. et al., 2001, MNRAS, 328, 17
Mattox J.R., Schachter J., Molnar L., Hartman R.C., Patnaik A.R., 1997, ApJ, 481, 95
McClure-Griffiths N., Green A., Dickey J., Gaensler B., Haynes R., Wieringa M., 2001, ApJ, 551, 394
Possenti A., Cerutti R., Colpi M., Mereghetti S., 2002, A&A, 387, 993
Roberts M.S.E., Romani R.W., Johnston S., Green A.J., 1999, ApJ, 515, 712
Roberts M.S.E., Romani R.W., Kawaii N., Gaensler B.M., Johnston S., 2001a, in Carramiñana A., Riemer O., Thompson D.J., eds, The Nature of Unidentified Galactic High-energy Gamma-ray Sources. Kluwer, Dordrecht, p. 135
Roberts M., Romani R., Johnston S., 2001b, ApJ, 561, L187
Safi-Harb S., Ogelman H., Finley J.P., 1995, ApJ, 439, 722
Sault R.J., Killeen N.E.B., 1998, The Miriad User's Guide. Australia Telescope National Facility, Sydney, http://www.atnf.csiro.au/computing/software/miriad/
Sault R.J., Staveley-Smith L., Brouw W.N., 1996, A&AS, 120, 375
Thompson D., 1998, in Shibazaki N., Kawai N., Shibata S., Kifune T., eds, Neutron Stars and Pulsars. Universal Academy Press, Tokyo p., 273
Tompkins W.F., 1999, PhD thesis Stanford Univ.
Whiteoak J.B.Z., 1993, PhD thesis, Univ. of Sydney
Whiteoak J.B.Z., Green A.J., 1996, A&AS, 118, 329
Whiteoak J.B.Z., Cram L.E., Large M.I., 1994, MNRAS, 269, 294

This paper has been typeset from a TEX/LATEX file prepared by the author.